

Constitutive and fracture behavior of ultra-strong supercrystalline nanocomposites ^{SCI}

Cite as: Appl. Phys. Rev. **8**, 031414 (2021); <https://doi.org/10.1063/5.0056616>

Submitted: 12 May 2021 • Accepted: 16 August 2021 • Published Online: 09 September 2021

 Büsra Bor,  Diletta Giuntini,  Berta Domènech, et al.



View Online



Export Citation



CrossMark

ARTICLES YOU MAY BE INTERESTED IN

Fast, accurate, point-of-care COVID-19 pandemic diagnosis enabled through advanced lab-on-chip optical biosensors: Opportunities and challenges

Applied Physics Reviews **8**, 031313 (2021); <https://doi.org/10.1063/5.0022211>

Combining nanosized elementary building blocks of soft and hard matter to create strong, damage resistant materials

Scilight **2021**, 371104 (2021); <https://doi.org/10.1063/10.0006368>

Anisotropic non-split zero-energy vortex bound states in a conventional superconductor

Applied Physics Reviews **8**, 031417 (2021); <https://doi.org/10.1063/5.0055839>



Applied Physics
Reviews

Read. Cite. Publish. Repeat.

19.162

2020 IMPACT FACTOR*



Constitutive and fracture behavior of ultra-strong supercrystalline nanocomposites

Cite as: Appl. Phys. Rev. **8**, 031414 (2021); doi: [10.1063/5.0056616](https://doi.org/10.1063/5.0056616)

Submitted: 12 May 2021 · Accepted: 16 August 2021 ·

Published Online: 9 September 2021












View Online



Export Citation



CrossMark

Büsa Bor,^{1,a)}  Diletta Giuntini,^{1,2,a)}  Berta Domènech,^{1,a)}  Alexander Plunkett,^{1,a)}  Michael Kampferbeck,^{3,a)}  Tobias Vossmeier,^{3,a)}  Horst Weller,^{3,a)}  Ingo Scheider,^{4,a)}  and Gerold A. Schneider^{1,b)} 

AFFILIATIONS

¹Institute of Advanced Ceramics, Hamburg University of Technology, Denickestrasse 15, D-21073 Hamburg, Germany

²Department of Mechanical Engineering, Eindhoven University of Technology, P.O. Box 513, 5600 MB Eindhoven, The Netherlands

³Institute of Physical Chemistry, University of Hamburg, Grindelallee 117, 20146 Hamburg, Germany

⁴Institute of Material Systems Modeling, Helmholtz-Zentrum Hereon, Max-Planck Straße 1, 21502 Geesthacht, Germany

^{a)}Electronic addresses: buesra.bor@tuhh.de; diletta.giuntini@tuhh.de; d.giuntini@tue.nl; berta.domenech@tuhh.de; alexander.plunkett@tuhh.de; michael.kampferbeck@chemie.uni-hamburg.de; tobias.vossmeier@chemie.uni-hamburg.de; horst.weller@chemie.uni-hamburg.de; and ingo.scheider@hereon.de

^{b)}Author to whom correspondence should be addressed: g.schneider@tuhh.de. Tel.: +49 40 42878 3037

ABSTRACT

Supercrystalline nanocomposites are a new class of hybrid and nanostructured materials that can reach exceptional mechanical strength and can be fabricated at low temperatures. Hierarchically arranged, they bridge the gap from the nano- to the macro-scale. Even though their mechanical properties are starting to be characterized, their constitutive behavior is still largely unexplored. Here, the mechanical behavior of supercrystalline nanocomposites of iron oxide nanoparticles, surface-functionalized with oleic acid and oleyl phosphate ligands, is investigated in both bending and compression, with loading–unloading tests. A new bar geometry is implemented to better detect deformation prior to unstable crack propagation, and notched bending bars are tested to evaluate fracture toughness. Micro-mechanical tests result in the values of strength and elastic modulus that are extremely high for supercrystals, reaching record-high numbers in the oleic acid-based nanocomposites, which also show a significant tension–compression asymmetry. The constitutive behavior of both materials is predominantly linear elastic, with some more marked nonlinearities arising in the oleyl phosphate-based nanocomposites. The fracture toughness of both types of nanocomposites, $\sim 0.3 \text{ MPa}\sqrt{\text{m}}$, suggests that extrinsic toughening, associated with both material composition and nanostructure, plays an important role. Fractographic observations reveal analogies with shear and cleavage in atomic crystals. The influence of material composition, nanostructure, and processing method on the mechanical behavior of the nanocomposites is analyzed.

© 2021 Author(s). All article content, except where otherwise noted, is licensed under a Creative Commons Attribution (CC BY) license (<http://creativecommons.org/licenses/by/4.0/>). <https://doi.org/10.1063/5.0056616>

INTRODUCTION

Nanoarchitected composites and hybrid materials are promising candidates for the next generation of multifunctional materials. Since new synthesis, processing, and characterization technologies have started to enable a better understanding and control of materials at the nanoscale level, it has become possible to design new materials by arranging nano-building blocks into micro- and macrostructures that foster emergent properties, unseen in the corresponding bulk counterparts.^{1–3} Particularly promising nanoarchitected materials are supercrystalline nanocomposites. They typically consist of metallic or

ceramic nanoparticles (NPs), surface-functionalized with organic ligands and arranged in periodic structures, reminiscent of atomic crystals.^{2–4} This combination of nano-sized elementary building blocks and their long-range order arrangement in a superlattice (with tunable interparticle distances) results in a broad set of functionalities, with applications in optoelectronics, magnetic devices, catalysis, batteries, and many more.^{2,5–8}

A largely unexplored aspect of supercrystalline nanocomposites is their mechanical behavior. Assessing and optimizing the mechanical properties of these materials is, however, relevant not only to guarantee

their structural integrity for implementation into devices, but also to enable potential new applications as bioimplants and bioinspired structural materials.^{1,3,9} Many materials found in nature feature outstanding combinations of mechanical properties that are achieved through nanostructures that are very similar to the ones defining supercrystals: tightly packed mineral NPs interfaced by a thin layer of organic material.^{10–12} By tailoring the composition and structure of nanocomposites along the design principles learned from nature, new materials with optimized combinations of strength, stiffness, hardness, toughness, and density can be developed.¹³

Supercrystalline nanocomposites can be produced with a variety of constituents, and great progress is being made in gaining control over the self-assembly process to achieve the desired superlattice structure.^{14–21} How this variety of compositions and nanostructures correlates with the material's mechanical behavior is nevertheless not always clear. The mechanical properties of supercrystals are usually assessed in terms of elastic modulus and hardness, via atomic force microscopy or nanoindentation of 2D films or 3D micro-supercrystals,^{22–25} with a few exceptions involving larger-scale superstructures.^{20,26} *In situ* x-ray scattering studies combined with hydrostatic pressing have also been performed, revealing a remarkable resistance to compression of many supercrystalline systems.^{27,28} All these investigations generally agree on the importance of ordered superlattices^{25,29} and of the crystallinity and faceting of the constituent NPs³⁰ in enhancing the nanocomposites' mechanical response with respect to their disordered counterparts. The role played by the organic ligands is instead multifold and not yet univocally clarified since many concurrent factors can coexist, such as chemical structure, ligand amount, grafting density, interdigitation, bending, or distribution in the interstitial sites.^{31–34}

An important aspect has however emerged when it comes to the role of the organic phase: if the ligands undergo a crosslinking reaction, leading to the formation of covalent bonds among neighboring organic chains, a remarkable enhancement of the mechanical properties is achieved.^{35–41} Thanks to the high confinement of the ligands into sub-nm interfaces and their crosslinking, the organic phase reaches very high values of strength (900 MPa in tension) and stiffness (elastic modulus of 13 GPa), which is consistent with analytical calculations based on density functional theory (DFT) results as well as with finite element simulations.^{3,35,42} This in turn greatly boosts the nanocomposites' macroscopic response, attaining elastic modulus and hardness values above 60 and 4 GPa, respectively.³⁶

To better grasp the overall mechanical behavior of these crosslinked supercrystalline nanocomposites, micro-compression and micro-bending tests are of great value. Analogous tests on biological nanostructured composites and polymer–ceramic nanocomposites with high ceramic content have shown high levels of strength and varying responses in different loading conditions, an aspect still to be better understood for supercrystals.^{43,44} Also, it is known that the addition of an organic phase into ceramic materials typically has a toughening effect.⁴⁵ The fracture toughness of supercrystalline materials has however been evaluated only via nanoindentation-based methods,^{36,46} again with outcomes indicating a superiority of the crosslinked nanocomposites, which feature values one order of magnitude higher than non-crosslinked supercrystals and theoretical predictions. The more reliable methods based on bending of notched bars are yet to be implemented.

This work applies, to the best of the authors' knowledge for the first time, loading–unloading micro-bending and micro-compression

testing methods to ultra-strong crosslinked supercrystalline nanocomposites, with a new design of bending bars aimed at more reliably assessing whether nonlinear deformations or stable crack growth occur. Fracture toughness is also assessed with micro-bending of pre-notched bars.

Two different material systems are considered: iron oxide NPs surface-functionalized either with oleic acid ($C_{18}H_{34}O_2$) or with oleyl phosphate ($C_{18}H_{37}O_4P$). Since the crosslinking of the organic phase is ultimately responsible for the nanocomposites' mechanical properties, all materials are tested in their crosslinked state.^{35–41} Extremely high values of strength and stiffness emerge, both in compression and in tension and for both material systems, while fracture toughness is confirmed to reach remarkably high values. Multiple mechanisms are found to control the nanocomposites' non-time-dependent mechanical response.

RESULTS

Organic content and nanostructure

Supercrystalline nanocomposites are obtained from two materials systems: (1) iron oxide NPs (Fe_3O_4) functionalized with oleic acid (OA), with radius 8.0 ± 1.3 nm, and (2) Fe_3O_4 NPs functionalized with oleyl phosphate (OPh) (radius 8.4 ± 1.0 nm). Oleic acid (OA) and oleyl phosphate (OPh) are organic ligands with identical aliphatic chains, but either a carboxylic acid or an ester of phosphoric acid, respectively, as anchoring groups on the NPs' surfaces. OA-based systems are more widely investigated,^{35–39,42,47} but the OPh ligands show potential for a further increase in strength. Phosphonic acids, indeed, are known to form stronger bonds on titania (TiO_2) with respect to their carboxylic acid counterparts (adsorption energies of 2.7 eV per bidentate bond compared to 1.6–1.8 eV for carboxylic acids),^{48–50} and density functional theory (DFT) computations suggest that the bonding of carboxylic acids to magnetite surfaces is $\sim 10\%$ – 20% stronger than to titania surfaces.⁵¹

To obtain bulk supercrystalline nanocomposites, the NPs are arranged into a face-centered cubic (FCC) structure (superlattice) via self-assembly. The self-assembled materials are then pressed uniaxially at $150^\circ C$ in a rigid die to obtain mm-size pellets, which are finally subjected to a heat treatment at $325^\circ C$ in inert atmosphere (see Experimental section). The heat treatment induces the crosslinking of the organic ligands, which leads to a significant mechanical strengthening, hardening, and stiffening.^{35,36} Figure 1 shows the nanostructure of the two types of supercrystalline nanocomposites (Fe_3O_4 –OA and Fe_3O_4 –OPh) after heat treatment. The long-range order superlattice can be clearly identified in both fracture surfaces. Alterations induced by the heat treatment are beyond the scanning electron microscopy (SEM) resolution, but previous *in situ* TEM studies indicate that there is no NPs faceting occurring up to $325^\circ C$.⁴⁰ Table I summarizes experimental organic contents of starting suspensions and bulk materials after heat treatment at $325^\circ C$ [measured with elemental analysis (EA)], together with superlattice constants [measured with small-angle x-ray scattering (SAXS)] and interparticle distances of the two material systems, also after heat treatment at $325^\circ C$.

The thermogravimetric analysis (TGA) of the starting suspensions indicates that both materials have similar decomposition modes under increasing temperature (see the supplementary material Chapter S1 and Fig. S1). The weight loss with temperature is more pronounced for Fe_3O_4 –OA than for Fe_3O_4 –OPh, and the decomposition

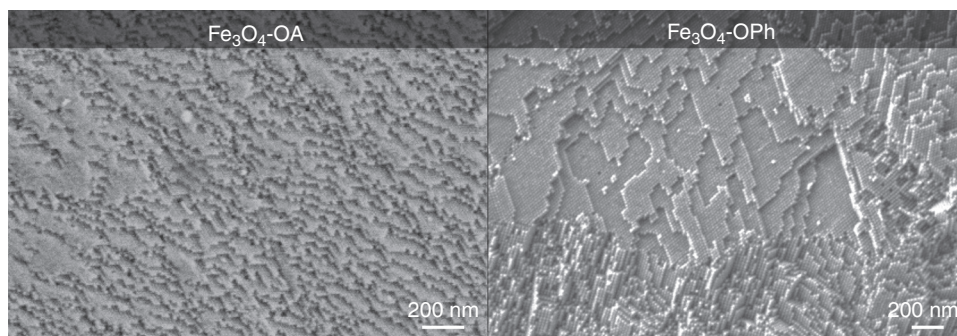


FIG. 1. SEM images of fracture surfaces of the Fe_3O_4 -OA (magnetite nanoparticles, NPs, surface functionalized with oleic acid) and Fe_3O_4 -OPh (magnetite NPs, surface functionalized with oleyl-phosphate) nanocomposites after heat treatment at 325°C . The long-range order nanostructure (superlattice, FCC-type) can be observed in both types of materials.

seems to start at lower temperatures. Elemental analysis (EA) indicates that the wt. % of organic ligands for the heat-treated materials is lower than in the suspensions of functionalized Fe_3O_4 NPs. The observed reduction is of 42% for Fe_3O_4 -OA and 24% for Fe_3O_4 -OPh. This is in agreement with the earlier decomposition of OA observed via TGA, as well as with the final organic content values, 7.7 and 9.5 wt. % for Fe_3O_4 -OA and Fe_3O_4 -OPh, respectively (see the [supplementary material](#) Table S1, Fig. S1, and Chapter S2). These results indicate that the heat treated Fe_3O_4 -OA materials contain a lower amount of organic phase compared to the heat treated Fe_3O_4 -OPh.

Small angle x-ray scattering (SAXS) indicates that both NP batches have similar and narrow monomodal size distribution (see the [supplementary material](#) Chapter S3 and Fig. S2). It also reveals that both types of nanocomposites consist of NPs arranged in face-centered cubic (FCC) superlattices.^{37,40} For Fe_3O_4 -OPh samples, the interparticle distance, ID , and superlattice constant, a , depend on whether they are measured parallel or perpendicular to the direction of the load used to press the samples into pellets. When the sample was measured with beam parallel to the pressing direction, a single lattice parameter (26.1 nm) was obtained. On the other hand, when the sample was rotated 90° , an ellipsoidal shape of the Debye-Scherrer rings associated with two lattice parameters (24.3 and 26.5 nm) appeared. This superlattice anisotropy was not present in the non-pressed samples, indicating that the pressing step leads, in the OPh material system, to anisotropic superlattices with closer NP packing along the direction of the applied load.⁴⁰ Therefore, for Fe_3O_4 -OPh samples, two superlattice parameters (and thus two ID s) are obtained: $a = 26.3$ nm (average of the two measured lattice parameters in direction perpendicular to the applied load) and $a = 24.3$ nm in the parallel case. Isotropic superlattices are instead obtained for Fe_3O_4 -OA regardless of the incident x-ray beam direction (Table I). Further details about the SAXS characterization of the Fe_3O_4 -OPh samples can be found in Ref. 40.

TABLE I. Organic content of the Fe_3O_4 -OA and Fe_3O_4 -OPh starting suspensions and supercrystalline nanocomposites after heat treatment, and superlattice parameters of the nanocomposites after heat treatment. The measured organic content is obtained via elemental analysis (EA, [supplementary material](#) Table S1), and the superlattice parameters are obtained via small-angle x-ray scattering (SAXS).

Sample	Organic content (wt. %)		Lattice constant, a (nm)	Interparticle distance, ID (nm)
	Suspension	Bulk sample at 325°C		
Fe_3O_4 -OA	13.2	7.7	24.5	1.3
Fe_3O_4 -OPh—perpendicular to pressing direction	12.5	9.5	26.3	1.8
Fe_3O_4 -OPh—parallel to pressing direction	12.5	9.5	24.3	0.4

Based on these sets of TGA, EA, and SAXS data, one can safely consider that even after heat treatment at 325°C , an organic layer is present at the interfaces between the NPs (see also the [supplementary material](#) Table S1). Note that a recent *in situ* x-ray scattering/micro-compression study of this same group has confirmed the fundamental role of the crosslinked organic phase in the load carrying capabilities of these kinds of inorganic-organic supercrystalline nanocomposites. The load results to be homogeneously distributed on the inorganic NPs (at least down to the μm -scale) thanks to the organic phase itself.³⁸

All samples were then tested in micro-compression, micro-bending, and for fracture toughness via bending of notched micro-bars. Representative images of the tested micro-samples are shown in Fig. 2, while details on the testing parameters are given in the Experimental section and [supplementary material](#) Chapters S4–S9. Based on post-mortem analyses of the tested pillars and bars from this and previous studies,³⁵ we consider the focused ion beam (FIB)-induced damage and potential degradation of the organic ligands to be negligible for the purposes of this study. It should be kept in mind, however, that an influence of the FIB treatment on the mechanical properties of the supercrystals cannot be fully ruled out and should be investigated in future studies.

Micro-compression

Micro-pillars were prepared by focused ion beam (FIB) and tested in a nanoindenter equipped with a diamond flat punch. Micro-pillars of crosslinked (heat-treated) supercrystalline nanocomposites, Fe_3O_4 -OA and Fe_3O_4 -OPh, were compressed uniaxially in loading-unloading cycles with increasing maximum load (see the Experimental section). The micro-compression data were corrected for the indentation of the pillars into the underlying bulk

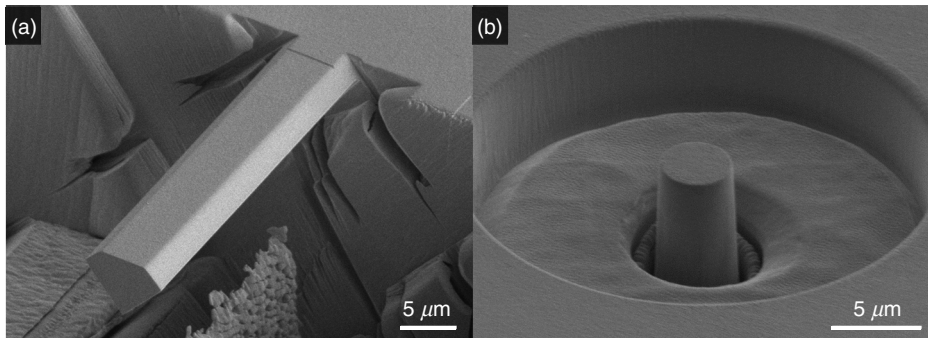


FIG. 2. Examples of micro-bending and micro-compression samples (bars and pillars), as obtained via focused ion beam (FIB). (a) Pentagon cross-sectioned bending bar made in $\text{Fe}_3\text{O}_4\text{-OA}$ supercrystalline nanocomposite, notched for fracture toughness evaluation. (b) Pillar made in $\text{Fe}_3\text{O}_4\text{-OPh}$ nanocomposite.

material and for thermal drift effects (see the [supplementary material](#) Chapter S6).

Figure 3 shows stress–strain curves and micrographs of pillars after fracture, for $\text{Fe}_3\text{O}_4\text{-OA}$ [Figs. 3(a) and 3(b)] and $\text{Fe}_3\text{O}_4\text{-OPh}$ [Figs. 3(c) and 3(d)]. The response of a representative pillar for each material system is shown in Figs. 3(a) and 3(c), respectively. The stress–strain curves of each cycle follow the same path, suggesting that

the variation of the loading rate has no effect on the mechanical response of the material, and no permanent deformation can be detected between each cycle. The rising slopes for the first three loading cycles in the case of $\text{Fe}_3\text{O}_4\text{-OA}$ are attributed to increased contact between pressing punch and pillar (alignment happens in the first cycle). Since for each individual pillar the stress–strain curves at each cycle mostly overlap, the last cycles of different pillars are compared

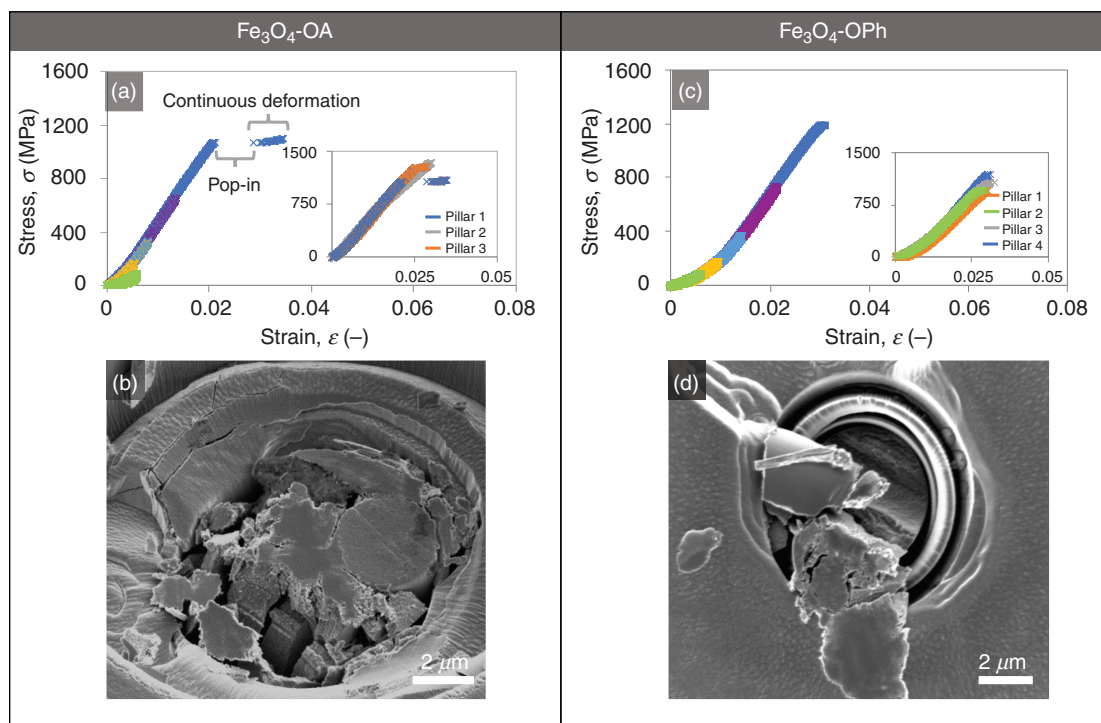


FIG. 3. Mechanical and fracture behavior of [(a) and (b)] $\text{Fe}_3\text{O}_4\text{-OA}$ and [(c) and (d)] $\text{Fe}_3\text{O}_4\text{-OPh}$ micro-pillars under uniaxial cyclic compressive loading. In (a) the loading–unloading cycles (indicated by the different colors) of a representative micro-pillar are shown, together with the curves of last cycles of different micro-pillars in the insets, for $\text{Fe}_3\text{O}_4\text{-OA}$. The stress–strain curves of each cycle mostly overlap, with the exception of the first cycle, during which punch–pillar alignment takes place. The increasing slopes of the first three cycles are attributed to the improved contact between flat punch and the pillar surface. Discontinuities in the last cycles are associated with slip and fracture events. (b) shows a postmortem micrograph of Pillar 1 in $\text{Fe}_3\text{O}_4\text{-OA}$. The fact that the top surface of the pillar lays off-center suggests that the failure started along a shear plane. (c) shows the loading–unloading cycles of a representative pillar, together with the curves of last cycles of different pillars in the inset, for $\text{Fe}_3\text{O}_4\text{-OPh}$. Nonlinear behavior appears in the early stages of compression, more markedly than in the case of $\text{Fe}_3\text{O}_4\text{-OA}$. (d) is a representative postmortem image of a $\text{Fe}_3\text{O}_4\text{-OPh}$ pillar (Pillar 2). Shear planes can be visualized. The fracture surfaces together with the stress–strain curves imply a slightly softer mechanical response in the $\text{Fe}_3\text{O}_4\text{-OPh}$ nanocomposites compared to the $\text{Fe}_3\text{O}_4\text{-OA}$ system.

and shown in the insets of Figs. 3(a) and 3(c). The curves for different pillars show a very good reproducibility in both materials.

The compressive strength of $\text{Fe}_3\text{O}_4\text{-OA}$ results to be 1222 ± 128 MPa, a record high value for supercrystalline nanocomposites,³⁵ while the elastic modulus is 47 ± 3 GPa. The strain at failure is $\sim 2\text{--}3\%$, with a mostly linear elastic behavior up to the fracture point. Some deviations from linearity appear, either as slope changes (Pillar 2), or in the form of displacement discontinuities (pop-ins) at $\sim 2\%$ strain, see Fig. 3(a) inset. These discontinuities indicate slip or fracture, after which the material keeps straining under constant load, suggesting a continuous inelastic deformation before the final catastrophic failure. These differences in the failure mechanisms are attributed to varying supercrystalline orientations of the tested areas. Since the material is poly-supercrystalline, the FCC slip planes—{111} family—are not always oriented in directions favorable for slip with respect to the applied load. A representative postmortem micrograph of a $\text{Fe}_3\text{O}_4\text{-OA}$ pillar (Pillar 1) is shown in Fig. 3(b). The material's supercrystallinity can be observed in the fracture surface [see also the supplementary material Fig. S3(b)]. There is no sign of cross section widening of the top surface of the pillar, and evaluation with an image processing tool (ImageJ⁵²) showed the top diameter stayed constant throughout the compression event. The intact pillar top surface indicates that the failure did not start from the top, but from below, and the postmortem position of the top surface (laying off-center from the base) indicates that the pillar failed by gliding along a shear plane. The pop-in event and the following continuous deformation [Fig. 3(a)] also point toward such a failure mechanism.

The compressive strength of $\text{Fe}_3\text{O}_4\text{-OPh}$ is 1046 ± 95 MPa with $\sim 3\%$ strain at failure, while the elastic modulus is 39 ± 3 GPa, which are also remarkably high values. The stress-strain curves here show initially a nonlinear elastic behavior, with material stiffening until $\sim 1.2\%$ strain, and then following a linear trend until $\sim 3\%$ strain, with slight nonlinearities appearing again right before failure [Fig. 3(c)]. Based on postmortem fracture surfaces [Fig. 3(d) shows an example], it can be stated that the failure of $\text{Fe}_3\text{O}_4\text{-OPh}$ pillars does not usually occur along a defined shear plane. Both fracture surface morphology and nonlinearities in the stress-strain curves suggest a slightly softer mechanical response of the $\text{Fe}_3\text{O}_4\text{-OPh}$ nanocomposites with respect to $\text{Fe}_3\text{O}_4\text{-OA}$. In the Discussion section, these observations are correlated with superlattice structure and organic ligands' behavior.

Micro-bending

Micro-bars, also prepared via FIB in bulk samples, were tested in bending in the same nanoindenter with a Berkovich tip. The bars have a pentagon-shaped cross section, to maximize stable crack growth (see the supplementary material Chapter S5). The raw displacement data are corrected for the tip's indentation into the bars' surfaces (see Experimental section) and thermal drift (see the supplementary material Chapter S6).

The micro-bending stress-strain curves and corresponding bars' fracture surfaces are shown in Fig. 4 for $\text{Fe}_3\text{O}_4\text{-OA}$ [Figs. 4(a)–4(d)] and $\text{Fe}_3\text{O}_4\text{-OPh}$ [Figs. 4(e)–4(g)]. Here, too, loading-unloading tests were performed. The figure shows, for both materials, a representative bar's stress-strain curve with all five cycles [Figs. 4(a) and 4(e)], the last cycle for all bars in the inset of the respective figures, and postmortem micrographs of the bars after failure [Figs. 4(b)–4(d) and Figs. 4(f)

and 4(g)]. For both materials, the curves overlap with a linear elastic behavior, until the bar starts to yield and fracture.

The $\text{Fe}_3\text{O}_4\text{-OA}$ supercrystalline nanocomposites have elastic modulus in bending of 70 ± 9 GPa and bending strength of 389 ± 25 MPa (see the supplementary material Chapter S5). The strain at failure is $\sim 0.6\%$, one order of magnitude lower than in compression. The difference between the elastic modulus under bending and compression (50% higher in bending) indicates a tension-compression asymmetry in the material behavior. If two different elastic stiffnesses are then considered for tension (E_T) and compression (E_C), with E_C obtained from the compression tests, one gets $E_T = 146 \pm 43$ GPa, which is a factor of 3 higher than the compressive stiffness (see the supplementary material Chapter S7). The tensile strength then becomes 575 ± 91 MPa. Note that the position of the bars' neutral axis is also corrected accordingly.

It is interesting to correlate stress-strain curves of the different bars with the respective fracture surfaces. Bar 1 shows the most marked nonlinearity in the stress-strain behavior, as highlighted in Fig. 4(a). In Fig. 4(b), the micrograph of Bar 1 shows an upper area in the fracture surface which is rich in organic material, from which it is likely that multiple small discrete crack jumps originated, until $\sim 0.4\%$ strain, followed by stable crack growth of one “macrocrack” until failure. A defect of smaller size, also attributed to an organic-rich cluster, is observed in Bar 2 [Fig. 4(c)]. Bar 3, instead, does not present defects that are detectable with the given SEM resolution and features indeed the highest bending strength [Fig. 4(d)]. Remarkably, the same Bar 3 had been notched to be tested for fracture toughness. However, as Fig. 4(d) shows, the notch resulted not to be deep enough to become critical for the bar's failure, which instead fractured at the fixed end, which is also a stress concentration. These considerations on critical defect size are applied in the section titled Fracture toughness section to analyze the material's fracture toughness.

The $\text{Fe}_3\text{O}_4\text{-OPh}$ supercrystalline nanocomposites, on the other hand, have elastic modulus in bending of 36 ± 1 GPa and bending strength of 338 ± 26 MPa, with $\sim 0.94\%$ strain at failure. These values imply a less stiff and strong material even though slightly more deformable before failure, compared with the $\text{Fe}_3\text{O}_4\text{-OA}$ nanocomposites. The tension-compression asymmetry is negligible. The bars break at their fixed end, and the supercrystalline structure is clearly visible in the fracture surfaces [Figs. 4(f) and 4(g)]. The fractures follow a less straight path through the bars' cross sections compared to the oleic acid-based material, which is likely connected to the overall higher strains to failure. No obvious pre-existing defect serving as crack nucleation site can be identified, and accordingly, the stress-strain curves of the bars are almost overlapping.

Fracture toughness

The fracture toughness tests were conducted analogously to the micro-bending tests, but on notched bars. To estimate the geometry factor needed for fracture toughness evaluation [see Eqs. (5) and (6) in the Experimental section], a rectangular cross section area, equivalent to the pentagon-shaped one (same cross section area and crack front width), was identified (see the supplementary material Chapter S8). This approximation was validated with a numerical simulation (see the supplementary material Chapter S9). All testing parameters are given in the supplementary material Table S5.

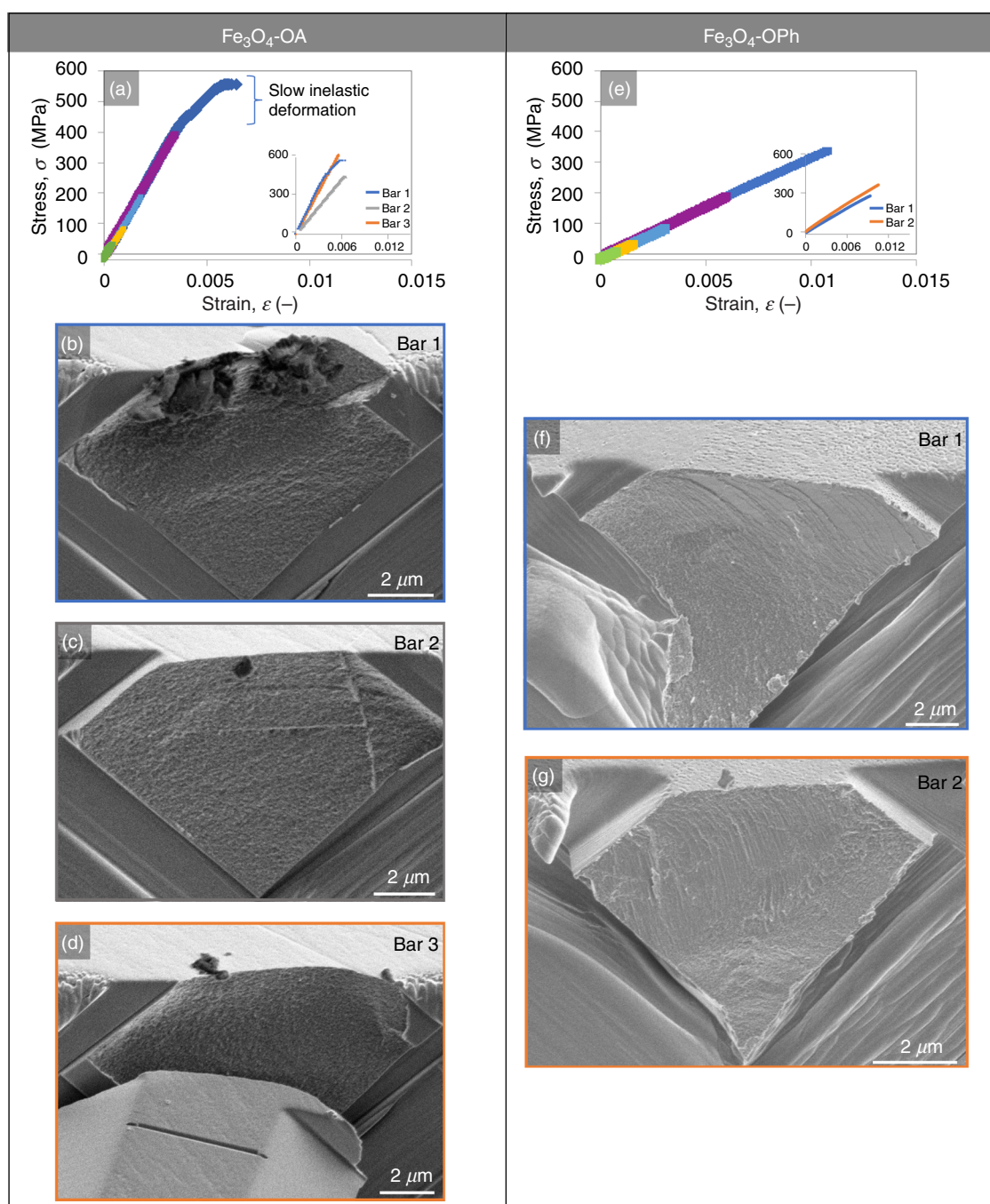


FIG. 4. Mechanical and fracture behavior of [(a)–(d)] $\text{Fe}_3\text{O}_4\text{-OA}$ and [(e)–(g)] $\text{Fe}_3\text{O}_4\text{-OPh}$ micro-bars under cyclic bending loading. In (a) the loading–unloading cycles (indicated by the different colors) of a representative bar of $\text{Fe}_3\text{O}_4\text{-OA}$ are shown together with the curves of last cycles of bars in the inset. Nonlinear behavior appears in the last loading cycle of a $\text{Fe}_3\text{O}_4\text{-OA}$ bar. Parts (b)–(d) show postmortem micrographs of broken bars of $\text{Fe}_3\text{O}_4\text{-OA}$. Bar 1 has an extended organic-rich area on the top of its cross section, associated with a significant nonlinearity in the stress–strain graph, indicating multiple small discrete crack propagation events. Bar 2 has a smaller defect compared to the Bar 1 and fails in a brittle manner according to the stress–strain curve. Bar 3 was originally produced for the assessment of fracture toughness; however, the notch was not deep enough to start the failure. The clean fracture surface indicates a brittle behavior, and the bar shows the highest measured bending strength, thanks to the absence of defects detectable at this scale. Part (e) shows the loading–unloading cycles of a representative bar, together with the curves of last loading cycles of all bars in the inset, for $\text{Fe}_3\text{O}_4\text{-OPh}$ nanocomposites. The stress–strain curves exhibit a higher strain and lower bending strength, which leads to a lower elastic modulus compared to $\text{Fe}_3\text{O}_4\text{-OA}$. Parts (f) and (g) show the fracture surfaces of Bar 1 and Bar 2 for $\text{Fe}_3\text{O}_4\text{-OPh}$. In the $\text{Fe}_3\text{O}_4\text{-OA}$ bars, the above-mentioned defects of different sizes likely acting as fracture nucleation sites can be visualized, while the $\text{Fe}_3\text{O}_4\text{-OPh}$ fracture surfaces show a more distorted morphology.

The Fe_3O_4 -OA supercrystalline nanocomposites have a fracture toughness of $0.30 \pm 0.04 \text{ MPa}\sqrt{\text{m}}$ (the stress at failure of the notched bars is $215 \pm 50 \text{ MPa}$). The postmortem fracture surfaces of the notched bars are shown in Figs. 5(a) and 5(b). The tested bars, Bars 1 and 2, had slightly different notch depths (~ 0.49 and $\sim 0.69 \mu\text{m}$, respectively), and, as expectable, Bar 2 failed at a lower stress value, even if with a comparable strain. Note that the indented imprint on the top surface of Bar 2 occurred after the bar's failure since in load-controlled nanoindentation the indenter's tip keeps loading until the pre-set load is reached.

If now one takes another look at Fig. 4 for Fe_3O_4 -OA, additional considerations on fracture toughness can be drawn. Bar 1 has an organic-rich area in the upper part, with an extension that resembles the one of the artificially introduced notches. By considering the depth of such a defect ($1.71 \mu\text{m}$), we obtain a fracture toughness value for this specific bar of $0.85 \text{ MPa}\sqrt{\text{m}}$. The higher value with respect to the ones calculated for the bars of Figs. 5(a) and 5(b) is unsurprising since the organic-rich area in Bar 1 of Fig. 4 provides some cohesion. On the other hand, Bar 3 of Fig. 4(d) had initially been produced for the evaluation of fracture toughness, but it was subsequently considered for the bending strength analysis since it did not break at the FIB notch, but at its root instead. As anticipated above, this implies that the notch's depth was not sufficient to act as a critical defect for crack propagation. Based on the calculated average fracture toughness of $0.30 \pm 0.04 \text{ MPa}\sqrt{\text{m}}$, we therefore estimate that the notch depth here is lower than $0.80 \mu\text{m}$. Remarkably, the values of K_{Ic} measured here with the single-edge notched bending (SENB) method correlate very well with the ones obtained through the indentation crack length (ICL) method and with an energy-based method in a previous work of this same group.³⁶

The Fe_3O_4 -Oph nanocomposites have an almost equal fracture toughness of $0.29 \pm 0.03 \text{ MPa}\sqrt{\text{m}}$ (stress at failure $177 \pm 18 \text{ MPa}$). Figures 5(c) and 5(d) show the postmortem fracture surfaces of the notched bars [notch depths of 0.74 and $0.84 \mu\text{m}$ for Figs. 5(c) and 5(d), respectively]. Note that another notched bar had been fabricated for the fracture toughness evaluation. However, its cross section resulted to be affected by the presence of an organic-rich area and absence of supercrystallinity, and therefore it was not considered in the analysis. A micrograph of the bar is shown in the Discussion section, Fig. 6(c). On the fracture surface of Bar 1, the supercrystalline planes are clearly visible, radiating from the notch toward the bars' edges. Such fractography features are very reminiscent of the river patterns that characterize transgranular cleavage fracture in crystalline materials, which occurs along tightly packed planes in metals, analogous to the tightly packed supercrystalline planes seen here.⁵³ In both cases, the river lines mark the crack propagation direction.

DISCUSSION

The measured elastic moduli and strengths, in compression and in bending, and the fracture toughness of Fe_3O_4 -OA and Fe_3O_4 -Oph supercrystalline nanocomposites are summarized in Table II. The Fe_3O_4 -OA nanocomposites show mechanical properties that are consistently higher than those of Fe_3O_4 -Oph, with the only exception of fracture toughness, where the discrepancy is minor and falls within the data scatter range. We consider the following factors to rationalize the measured mechanical properties: superlattice parameters, organic phase content (wt. %), type of bonds in each ligand molecule, NP size, and self-assembly method applied to obtain the bulk nanocomposites.

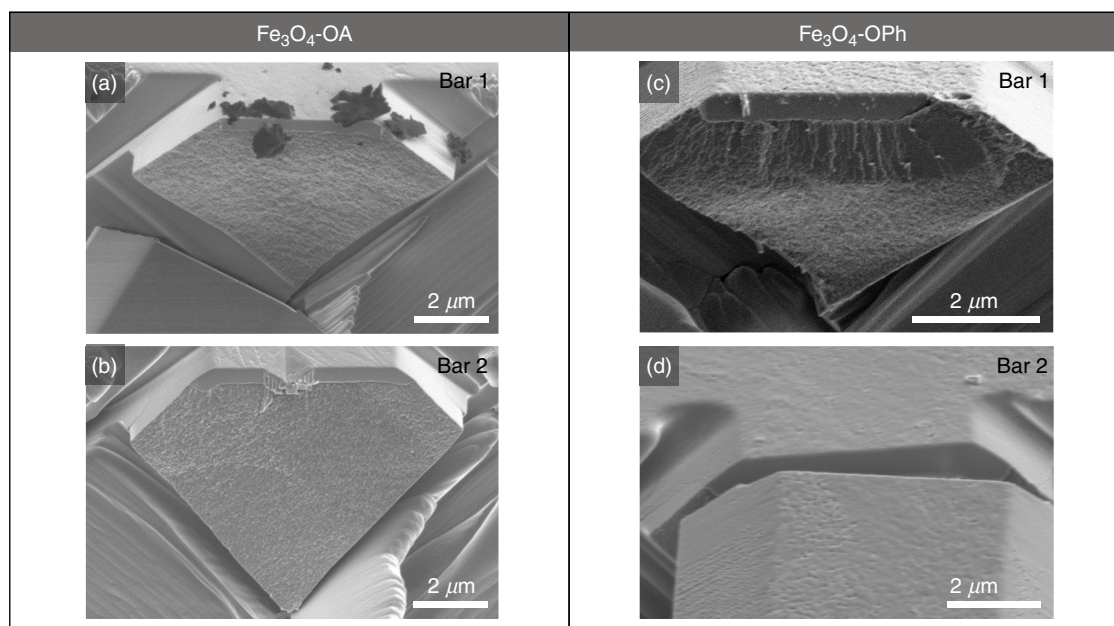


FIG. 5. Postmortem fracture surfaces of notched bending bars of [(a) and (b)] Fe_3O_4 -OA nanocomposites and [(c) and (d)] Fe_3O_4 -Oph nanocomposites. The pre-existing notches, fabricated at the FIB, can be distinguished by the smooth surface at the top of the cross sections as a result of the FIB process itself. The supercrystallinity of the fracture surfaces is also visible and particularly marked in part (c). In (c), a morphology analogous to the river patterns typical of transgranular cleavage fracture in crystalline materials is visible, extending right below the notch.

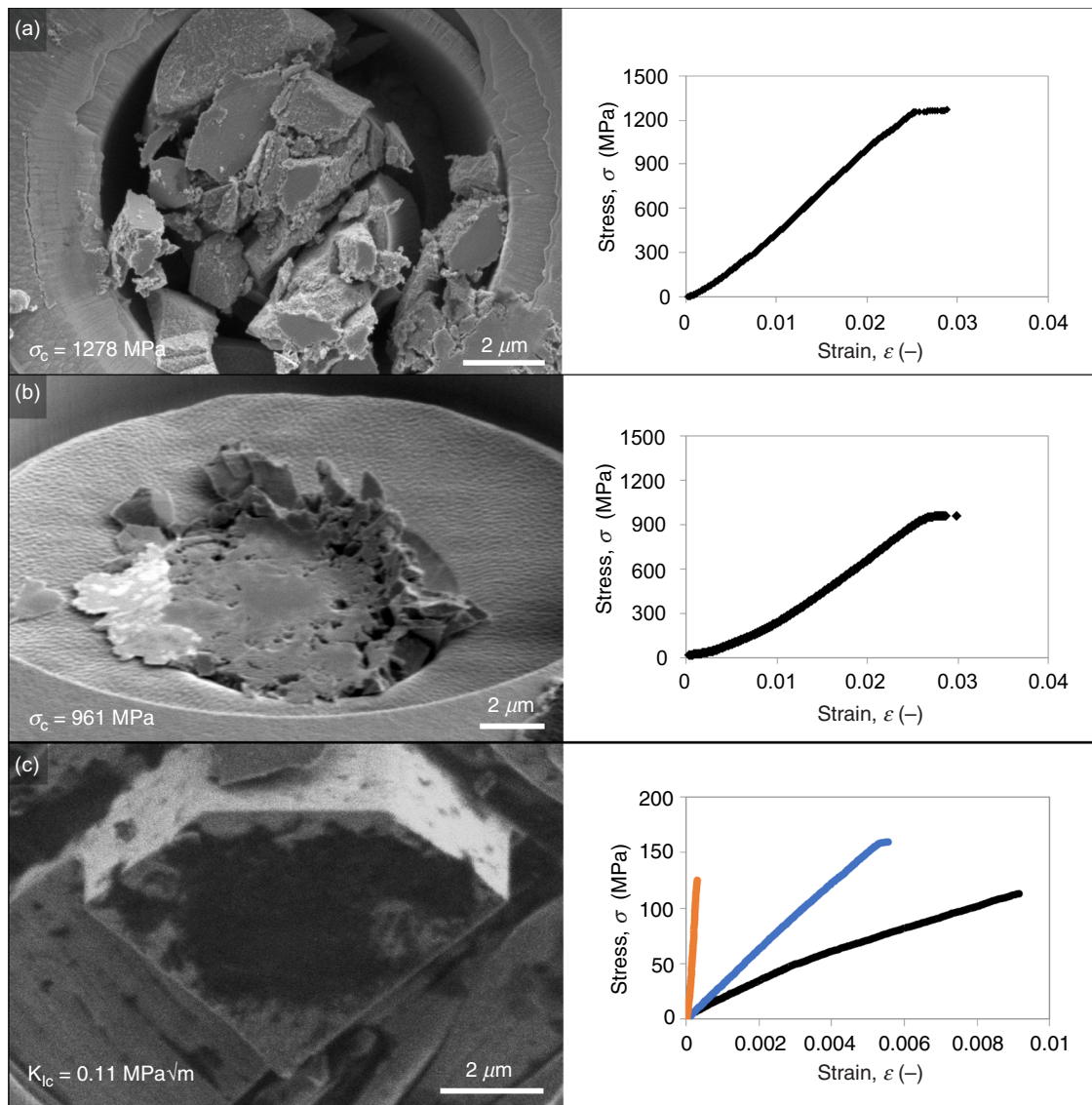


FIG. 6. Fracture surfaces of pillars and bars of the two material systems (OA- and OPh-based) after mechanical tests, with the respective stress–strain curves. (a) Fe₃O₄–OA pillar broken into multiple parts with sharp fracture surfaces. (b) Fe₃O₄–OPh pillar broken with a morphology that suggests a softer material response, corresponding to a non-linear trend in the stress–strain curves that is likely associated with the larger amount of organic material present in this material system when compared with the OA-based one. (c) Organic-rich fracture surface of a notched Fe₃O₄–OPh bar. The organic-rich bar (black curve, i.e., third curve from the left) strains more than the other bars, which exhibit supercrystalline fracture surfaces. Note that due to the internal structure and composition of the bar, i.e., not supercrystalline and organic-rich, the bar in (c) was not considered in the stress–strain behavior evaluation.

TABLE II. Summary of measured mechanical properties of Fe₃O₄–OA and Fe₃O₄–OPh supercrystalline nanocomposites.

Samples	Elastic modulus (GPa)		Strength (MPa)		Strain at failure (~%)		Fracture toughness (MPa√m)
	E_T	E_C	σ_T	σ_C	ε_T	ε_C	
Fe ₃ O ₄ –OA	146 ± 44 ^a	46 ± 3	575 ± 91 ^a	1222 ± 127	0.6	2.5	0.30 ± 0.04
Fe ₃ O ₄ –OPh	36 ± 1	38 ± 2	338 ± 26	1046 ± 94	0.9	3.0	0.29 ± 0.03

^aConsidering tension–compression asymmetry.

Interesting differences between bending and compression behavior are already observable within one single material system. The Fe_3O_4 -OA nanocomposites show significantly higher stiffness in bending than in compression, while the opposite holds for strength. We explain such a behavior with the deformation mechanisms of the organic phase and the material's sensitivity to defects. The crosslinked aliphatic chains that form the organic interphase are likely to behave like rigid springs when extended and pulled under tensile loads. The covalent bonds resulting from the crosslinking and the anchoring to the NPs, combined with the short length of the organic molecules, provide high stiffness. The chains' length is ≤ 2 nm at full extension before crosslinking,^{54,55} and it becomes shorter due to the decomposition of ligands with increasing temperature (see the [supplementary material](#) Fig. S1). On the other hand, the decreasing organic content (assessed via EA) is expected to leave hollow FCC superlattice interstitial sites (octahedral and tetrahedral).⁴² This implies that there is room for rearrangement of the organic phase upon compression, within the interfaces between NPs and in the interstitial sites, thus leading to a lower elastic modulus in compression with respect to the bending case. This effect is indeed amplified at the ligands' scale. Given the supercrystalline nanocomposites' strain, ε_{SC} , and the initial interparticle distances, with a simplified model of two layers of NPs interfaced by ligands (see the [supplementary material](#) Chapter S10), one can estimate interparticle distances and strains in the organic phase after deformation (tension or compression). For Fe_3O_4 -OA, strains in the organic phase are found to be 8% in tension and 33% in compression.

Strength, on the other hand, is highly sensitive to defects in tensile tests, while compressive loads are less critical from this viewpoint. It is well known how in brittle materials, due to their lack of plastic yielding ability, micro- or nano-cracks tend to become critical for failure when subjected to tensile loads.⁵⁶ A non-uniform distribution of the crosslinked organic phase, even at the nanoscale (e.g., in the form of localized absence of crosslinks, organic phase clusters, or superlattice defects—all known to affect supercrystalline nanocomposites)^{6,37} can behave as critical crack initiators during bending experiments. Under compressive loads, such nano-cracks do not grow, and to reach micro-pillars' failure, significant shear (or buckling) deformations need to occur, as the shear planes visible in [Fig. 2](#) confirm. It is therefore not surprising to detect a compressive strength that is more than two times higher than the tensile one.

It is also interesting to compare the measured strength values with the corresponding theoretical ones according to the estimations of Orowan and Frenkel.⁵⁶ The tensile strength of the Fe_3O_4 -OA supercrystals (~ 575 MPa) is ~ 80 times lower than their theoretical cleavage strength ($\sim E/\pi$, i.e., ~ 46 GPa), while the shear strength (half of the measured compressive strength, i.e., ~ 611 MPa) is only five times lower than the theoretical shear strength ($\sim G/5.1$, i.e., ~ 3 GPa). The shear modulus is calculated as $G = E/[2(1 + \nu)]$, with E as obtained from micro-compression tests and ν as calculated via finite element simulations in a previous work.⁴² Such ratios between theoretical and measured strengths are rather low, indicating that the tested micro-samples only contain few nano-sized defects and confirming that these become more critical in tensile loading conditions.

The Fe_3O_4 -Oph nanocomposites have a higher organic content (9.5 wt. %, see [Table I](#)) with respect to Fe_3O_4 -OA. As expectable, a higher amount of “soft” (even after crosslinking, and with respect to the inorganic NPs) organic phase is here associated with overall lower

mechanical properties. This effect appears to overrule the potential higher strength of the bond at the NP-ligand interfaces. The size of the NPs also changes between the two material systems, being slightly larger in the Fe_3O_4 -Oph system. Several contrasting hypotheses can be found in the literature on the role of NP size on supercrystals' elastic modulus and hardness.^{13,25,57} Here, however, the changes in NP sizes between the two batches are considered to be negligible, and thus no significant effect on the measured mechanical properties is anticipated. The same holds for the NP size distribution.

The Fe_3O_4 -Oph supercrystalline nanocomposites also show a higher level of nonlinearity and deformability before failure in their stress-strain curves. Higher strains to failure are consistently detected ([Table II](#)), and visual inspection of fractured bars and pillars also hints at some pre-failure material distortion, and at an overall “softer” response of the material, as the comparison between [Figs. 6\(a\)](#) and [6\(b\)](#) suggests (see also the [supplementary material](#) Chapter S11). In the compression curves of Fe_3O_4 -Oph pillars, nonlinearities are observed, similar to the ones reported for nanocomposites consisting of the same iron oxide NPs, but with polybutadiene as organic phase.^{19,44} A notched bar initially prepared in Fe_3O_4 -Oph is shown in [Fig. 6\(c\)](#) after fracture, with a large organic cluster visible in the cross section, and the corresponding stress-strain curve, showing much higher strain values with respect to the other two notched bars ([Fig. 5](#)). Such significant deformations again correlate well with the higher amount of ligand molecules. An additional factor to be kept in mind is the presence in the Oph molecules of a flexible ester bond, between anchoring group and aliphatic chain, which gives these ligands a higher deformability. It is finally worth mentioning explicitly that different self-assembly methods applied to obtain the two types of supercrystalline nanocomposites might also influence the ligands' conformation and presence of defects in the samples, affecting the final mechanical response. Solvent destabilization, used for Fe_3O_4 -OA nanocomposites, is expected to lead to higher-quality supercrystalline structures.

Another difference between Fe_3O_4 -OA and Fe_3O_4 -Oph nanocomposites is the absence of tension-compression asymmetry in the latter. We speculate that the lack of such asymmetry in the Fe_3O_4 -Oph system is due to its anisotropic superlattice constants. In the case of compression, the failure via shear cannot be directly correlated with a specific value of a , but for bending, it is important to know that the bars' axis was aligned with the direction of the short superlattice constant (24.3 nm). This means that the Oph ligands are confined in a very small interface (0.4 nm, instead of 1.3 nm in the OA case) along the loaded bar's length and, therefore, can be more easily stretched before they start opposing resistance to additional deformation. On the other hand, the interstitial sites are still available for the organic ligands' rearrangement in the section of the bar that is under compressive stresses. It is important to note here that these considerations on material stiffness and compression-tension asymmetry are based on assumptions on the conformation of the organic ligands at the NP-NP interfaces. These assumptions rely on SAXS data and previously published Energy-Dispersive X-ray spectroscopy (EDX) data on similar material systems,¹⁹ but can vary depending on material system and processing routine, even though it is worth mentioning here that such an asymmetry was also observed in a previous work of this group.³⁵ A more exact characterization of this asymmetry effect can be performed in future work, with a focus on its dependence on

interparticle distances, organic ligands' molecular length, and local superlattice orientation. The control of such nanostructural parameters during material processing therefore appears to become of great importance for the fine-tuning of the mechanical behavior of these kinds of nanocomposites and confirms the fundamental role played by the crosslinked organic phase.³⁸

As for strength, we find again a similar trend in the material's behavior in tension and compression (here too defects play a decisive role), but overall lower values with respect to $\text{Fe}_3\text{O}_4\text{-OA}$ (decrease in $\sim 41\%$ in tension and $\sim 14\%$ in compression). This effect is consistent with the higher organic content in the $\text{Fe}_3\text{O}_4\text{-OPh}$ nanocomposites. Additionally, the same considerations applied to the OA-based system on theoretical strength can be drawn here, and interestingly we find the same ratio between theoretical and measured values in compression (lower in the experimental by a factor of 5), and a factor of 34 in tension, consistent with the trend in elastic moduli.

Fracture toughness is the only measured mechanical property that results in the same values between $\text{Fe}_3\text{O}_4\text{-OA}$ and $\text{Fe}_3\text{O}_4\text{-OPh}$. These values, $\sim 0.3 \text{ MPa}\sqrt{\text{m}}$, are remarkably high for supercrystalline materials,^{36,44} but still mainly representative of brittle materials. In supercrystalline nanocomposites, fracture toughness results from small deviations (nanoscale) of crack paths around the inorganic NPs. Since these values are higher than theoretical predictions based on purely intrinsic toughening mechanisms, we assume that the organic ligands play a role toward extrinsic toughening. Indeed, addition of a thin layer of soft phase (such as the organic ligands in this work) and material nano- and/or micro-structuring are well-known strategies, largely learned from biomaterials,⁵⁸ toward toughening otherwise brittle materials. The higher amount of organic phase present in the OPh-based nanocomposites, and thus their higher potential to dissipate energy during fracture, can then explain how these manage to match the stronger OA materials in terms of fracture toughness. The above-mentioned theoretical predictions on the nanocomposites' intrinsic fracture toughness are based on a Barenblatt approach, applied to NPs bridged by aliphatic chains, and (as shown in Ref. 36) they lead to values that are one order of magnitude lower than the experimentally measured ones. Remarkably, the K_{IC} values obtained here via SENB method, considered among the most reliable methods, correlate rather well with the ones calculated in a previous work for $\text{Fe}_3\text{O}_4\text{-OA}$ via indentation crack length method ($0.21 \pm 0.03 \text{ MPa}\sqrt{\text{m}}$) and with an energy-based method ($0.5 \pm 0.3 \text{ MPa}\sqrt{\text{m}}$).³⁶ The small discrepancies are attributed to the assumptions that had to be made on the sub-surface crack path, and the value obtained here is considered to be the most accurate.

Even though the details on the role played by the organic phase in the supercrystalline nanocomposites' mechanical behavior should be explored further, some interesting aspects have emerged in this study. The combination of FCC superlattice and crosslinked and confined organic ligands leads to nanocomposites featuring mechanical behavior aspects of both brittle and ductile materials. A mainly brittle and ultra-strong response is observed in bending and compression conditions, but still the fracture toughness values are higher than theoretical predictions (see Barenblatt approach⁵⁹), inelastic pre-fracture deformations can occur, and shear and cleavage along tightly packed supercrystalline planes are detected. A secondary, and yet relevant, aspect of the outcomes reported in this study is the reduction in the data scatter that typically affects the mechanical testing of

supercrystals,^{23,24} which we associate with the improved nanocomposites' processing routine. Additional tests are expected to further reduce the scatter issue.

CONCLUSIONS

Supercrystalline hybrid inorganic–organic nanocomposites, consisting of iron oxide NPs that are surface-functionalized with oleic acid and oleyl phosphate ligands, all show remarkably high values of strength and elastic modulus in both bending and compression. Record-high values of compressive strength ($1.2 \pm 0.1 \text{ GPa}$) and bending modulus ($70 \pm 9 \text{ GPa}$) are found for the oleic acid-based nanocomposites, which also present a tension–compression asymmetry. Note that supercrystalline nanocomposites typically show the values of elastic modulus and hardness that are lower compared to the materials featured in this work and that this difference increases up to more than an order of magnitude when it comes to crosslinked materials.^{23,25,26,32,34–36,46,47,60} These broad ranges are due to the large data scatter that typically affects supercrystals,^{23,24} an effect that has been mitigated here and that we expect will be further reduced in future studies. These considerations all apply to the microscale, while efforts for material upscaling and assessment of macroscopic mechanical properties are ongoing. The oleic acid-based nanocomposites also present a marked tension–compression asymmetry. Such an asymmetry with an elastic modulus of 146 GPa in tension and 46 GPa in compression is likely the outcome of the limited extendibility of the ligands in tension, while their bending and confinement is possible within the inter-NP interfaces and interstitial sites. Inelastic deformation is mainly detected at the latest loading stages and is most probably due to cracking, either limited microcrack jumps or stable crack extension. The oleyl phosphate-based materials feature overall lower mechanical properties, larger strains to failure, and more marked nonlinearities in their stress–strain curves, attributed to the higher organic content. The fracture toughness, evaluated for the first time with notched bending bars in supercrystalline nanocomposites, results in values $\sim 0.3 \text{ MPa}\sqrt{\text{m}}$ for both material systems, which are well above the values that would be associated with purely intrinsic toughness due to inter-NP forces and are thus a strong hint that extrinsic mechanisms are contributing. Additional work is needed to elucidate the role played by organic ligands in the mechanical behavior of supercrystalline nanocomposites, especially in terms of their conformation and crosslinking, and to analyze the materials' time-dependent deformation mechanisms. Interesting future research directions can also involve the comparison between strength of supercrystalline and “superamorphous” nanocomposites, the role of NP size and of supercrystalline domains (grains) size, and more complex material systems.

EXPERIMENTAL

Material preparation

Iron oxide (Fe_3O_4) NPs functionalized with oleic acid (OA) (radius $8.0 \pm 1.3 \text{ nm}$) and iron oxide (Fe_3O_4) NPs functionalized with oleyl phosphate (OPh) (radius $8.4 \pm 1.0 \text{ nm}$) are the building blocks of the supercrystalline nanocomposites. The $\text{Fe}_3\text{O}_4\text{-OPh}$ system is obtained via the ligand exchange reaction starting from a $\text{Fe}_3\text{O}_4\text{-OA}$ system, as described in a previous study.⁴⁰ The functionalized NPs of both systems are initially suspended in toluene. The 3D bulk supercrystalline nanocomposites are obtained with a three-step process. First, the NPs form face-centered cubic (FCC) superlattices via

self-assembly (via solvent destabilization by slow diffusion of ethanol in the Fe_3O_4 -OA system³⁶ and via solvent evaporation for Fe_3O_4 -OPh^{19,40}). The dry self-assembled materials are subsequently pressed at 50 MPa and 150 °C, a temperature previously optimized to ensure suitable rheology of the ligands during compression.³⁵ The pressed materials are finally heat-treated at 325 °C under N_2 (g) to induce the ligands' crosslinking and thus the mechanical properties' enhancement (up to a three- or fourfold increase in the hardness, strength, and stiffness).^{35,36,40}

Composition and nanostructure characterization

The materials' nanostructure is imaged via scanning electron microscopy (SEM) at 1.5 kV, with 10 μm aperture size, in high vacuum mode. To do so, sample pieces are mounted on aluminum sample holders with silver glue (Acheson Silver DAG 1415M). The superlattice parameters and particle diameters are obtained via small-angle x-ray scattering (SAXS),^{39,40} performed at the high energy materials science (HEMS) beamline operated by Helmholtz-Zentrum Geesthacht at the PETRA III storage ring of the Deutsches Elektronen-Synchrotron (DESY).⁶¹ A Schulz-Zimm size distribution of the particle radius and number density-based fitting are used for the determination of the particle size.³⁷ The thermal decomposition of the starting suspensions is assessed via thermogravimetric analysis (TGA), performed with a Netzsch TGA 209 F1 Iris, 25–800 °C temperature range, and 5 K/min heating ramp at 60 ml N_2 flux. Elemental analysis of dried powders obtained from the starting suspensions as well as nanocomposites was performed on an Eurovector EuroEA3000 elemental analyzer (hydrogen, carbon) and, after pretreatment with nitric and perchloric acid for acid digestion, via inductively coupled plasma-atomic emission spectroscopy (ICP-AES) on a SPECTRO Analytical Instruments SPECTRO ARCOS system.

Preparation for micro-mechanical tests

The samples are then prepared for mechanical testing by embedding a portion of each sample (1–2 mm thick) in a cold curing acrylic mounting resin (Scandquick, Scan-DIA, Hagen, Germany) and polishing them down to a surface roughness of 50 nm by using silicon carbide (SiC) papers and diamond suspensions (for 15–0.25 μm from ATM GmbH, Germany and for 0.05 μm from Buehler, Germany). All samples are tested in the cross section (along the pressing axis).

Micro-bending bars and compression pillars are prepared using focused ion beam (FIB) milling with a gallium ion source (FEI Helios NanoLab G3, Thermo Fisher Scientific, Oregon, USA). The milling currents are 47 (rough cuts), 21 (finer cuts), and 2.5 nA (polishing) for the bars, and 2.5, 0.43, and 0.24 nA for the pillars. A pentagon-shaped cross section (as shown in Fig. 6) is chosen for the bars. This geometry allows minimizing unstable crack propagation by increasing the cross section the crack needs to extend into. The sizes of the pillars and bars are given in the [supplementary material](#) Tables S2, S3, and S5. Some bars are then notched by FIB to create a straight-through notch for the fracture toughness measurements.⁶² The notches are made in the proximity of the bars' bases, aiming at a depth of half the height of the upper (resistant) cross section. This is realized by multiple passes with 0.24 pA current to minimize the effects of the FIB's Gaussian shape, and the final notch depths are then verified after the bars have been broken ([supplementary material](#) Table S5).

Micro-mechanical tests

Micro-compression and micro-bending tests are performed in 5–6 loading–holding–unloading cycles until fracture to gain information on the nanocomposites' constitutive behavior and to monitor the onset and propagation of cracks. Note that even though the challenging nature of these micro-mechanical studies on supercrystalline nanocomposites limits the number of micro-pillars and bars that can be tested, a careful optimization of the sample preparation and testing procedures has enabled a significant decrease in the data scatter that typically characterizes the mechanical properties of these kinds of nanocomposites.^{23,35} Tests data were not included in the analysis when the tested area resulted to be non-supercrystalline (superamorphous, beyond the purposes of this study), as assessed after failure via SEM, or when technical difficulties arose during the loading itself, such as alignment issues in the nanoindenter. The tests are performed in loading control mode by doubling the load at each cycle. In each cycle, the loading and unloading rates are equal, and the time to load is maintained constant, resulting in an increase in the loading/unloading rate at each cycle. The loading rate of the first cycle is always 4×10^{-4} mN/s, and the holding time is 10 s. The tests started only when the thermal drift was < 0.05 nm/s. However, due to the long duration of each test (40–50 min/test), the measurements are still affected by the drift. An additional correction is therefore applied, as described in the [supplementary material](#) Chapter S6.

Bending and compression tests were carried out in a Nanoindenter G200 (Agilent, Santa Clara, CA, USA). Bending tests were performed with a Berkovich tip (Synton-MDP LTD, Port, Switzerland) to guarantee a fixed rigid contact, avoid torque, slip, and misalignment issues, and to be able to find the exact loading point in the bars after fracture^{63–65} (the nanoindenter's optical microscope allows tip positioning with an accuracy of ~ 1 μm). The raw displacement data are then corrected for the tip's indentation of the bars.⁶⁵ This correction was applied by subtracting the displacements measured during five cyclic indentations at the same loading rates in areas adjacent to the base of the bars. Uniaxial compression is performed using a diamond flat punch with a diameter of 10 μm (Synton-MDP LTD, Port, Switzerland). Here also the effect of the pillars' indentation in the substrate was considered, as detailed below.

The bending stresses, σ_B , of the bars are calculated as $\sigma_B = My/I$, where M is the bending moment, y is the distance of the neutral axis to the bar surface, and I is the moment of inertia. The corresponding strain is calculated as⁶⁶

$$\varepsilon_b = \frac{3 \delta y}{L^2}, \quad (1)$$

where ε_b is the bending strain at the upper surface, δ is the true bar deflection after the indenter displacement is subtracted, y is the distance from the neutral axis of the bar to the top of the bar, and L is the distance between the base of the bar and the loading point.

The compressive stress and strain of the pillars are calculated as⁴³

$$\sigma_c = \frac{4P}{\pi D_{av}^2} \quad (2)$$

and

$$\varepsilon_c = \frac{\delta}{h}, \quad (3)$$

where σ_c is the compressive stress, P is the load, D_{av} is the average diameter of each pillar (between top and bottom, considering the FIB-induced tapering), h is the pillar height, and δ is the true displacement, corrected from the total measured displacement δ_m by subtracting the indentation of the pillar into the underlying material, δ_s , as $\delta = \delta_m - \delta_s$. This correction follows the Sneddon's solution for a perfectly rigid cylindrical punch pressed into an elastic half-space,⁶⁷

$$\delta_s = \frac{1 - \nu^2 P_{max}}{E D}, \quad (4)$$

where E is the elastic modulus, assessed in the heat treated nanocomposites via nanoindentation (300 nm depth, Berkovich tip, continuous stiffness measurement (CSM) method), namely, 64.1 GPa for Fe₃O₄-OA and 75.4 GPa for Fe₃O₄-OPh, and ν is the Poisson's ratio, 0.34.^{36,42} The elastic moduli in bending and compression are then calculated from Hooke's law, as $E = \sigma/\epsilon$ in the linear elastic regime (also see the [supplementary material](#) Chapter S5).

To the best of our knowledge, there is no given equation in the literature for the fracture toughness and geometry factor estimation of bars with a pentagonal cross section. Therefore, as approximation, the fracture toughness is calculated by using the equation for rectangular cross sections with width and thickness such that the cross section area and the crack front width are equivalent to the pentagon case (see the [supplementary material](#) Chapter S8). This assumption has been validated in the [supplementary material](#) Chapter S9. The fracture toughness K_{Ic} is then found as⁶⁸

$$K_{Ic} = \frac{6P_{max}L}{b_{cal}w_{cal}^2} \sqrt{\pi a} f\left(\frac{d}{w_{cal}}\right), \quad (5)$$

where L is the distance between notch and loading point, d is the notch depth, $f(d/w_{cal})$ is the geometry factor, and b_{cal} and w_{cal} are the calculated width and thickness of the equivalent rectangle bar (given in the [supplementary material](#) Chapter S8). The geometry factor for a rectangular bar is given as⁶⁸

$$f\left(\frac{d}{w_{cal}}\right) = 1.13 + 1.374\left(\frac{d}{w_{cal}}\right) + 5.749\left(\frac{d}{w_{cal}}\right)^2 - 4.464\left(\frac{d}{w_{cal}}\right)^3. \quad (6)$$

AUTHORS' CONTRIBUTIONS

B.B., D.G., I.S., and G.A.S. designed the research and wrote the paper; B.B. and B.D. conducted the sample preparation; B.B. and D.G. performed the mechanical tests; B.B., D.G., and B.D. characterized the samples' nano- and micro-structures; M.K. synthesized OPh-modified nanoparticles and conducted the chemical characterization; T.V. and H.W. supervised the synthesis of nanoparticles and their chemical characterization; B.B., D.G., B.D., A.P., and M.K. analyzed the data; I.S. conducted the numerical simulations and asymmetry calculations; and G.A.S. supervised the study. All authors discussed the results and contributed to the manuscript writing. B.B. and D.G. contributed equally to this work.

SUPPLEMENTARY MATERIAL

See the [supplementary material](#) for supplementary paragraphs 1-11, supplementary figures S1-S9, and supplementary tables S1-S6.

ACKNOWLEDGMENTS

The authors gratefully acknowledge financial support from the Deutsche Forschungsgemeinschaft (DFG, German Research Foundation)—Project No. 192346071—SFB 986. B.B. gratefully acknowledges the support from the Ministry of National Education of the Republic of Turkey. D.G. gratefully acknowledges the support from the Alexander von Humboldt Foundation. The authors are very thankful to Kai Sellschopp (Hamburg University of Technology, TUHH) and Malte Blankenburg (Deutsches Elektronen-Synchrotron, DESY) for their valuable input on DFT and SAXS data.

DATA AVAILABILITY

The data that support the findings of this study are available from the corresponding author upon reasonable request.

REFERENCES

- ¹M. R. Begley, D. S. Gianola, and T. R. Ray, *Science* **364**, eaav4299 (2019).
- ²M. A. Boles, M. Engel, and D. V. Talapin, *Chem. Rev.* **116**, 11220 (2016).
- ³E. V. Sturm and H. Cölfen, *Crystals* **7**, 207 (2017).
- ⁴C.-W. Liao, Y.-S. Lin, K. Chanda, Y.-F. Song, and M. H. Huang, *J. Am. Chem. Soc.* **135**, 2684 (2013).
- ⁵L. Bergström, E. V. Sturm née Rosseeva, G. Salazar-Alvarez, and H. Cölfen, *Acc. Chem. Res.* **48**, 1391 (2015).
- ⁶D. V. Talapin, J.-S. Lee, M. V. Kovalenko, and E. V. Shevchenko, *Chem. Rev.* **110**, 389 (2010).
- ⁷T. Tachikawa and T. Majima, *NPG Asia Mater.* **6**, e100 (2014).
- ⁸M. P. Pileni, *J. Phys. Chem. B* **105**, 3358 (2001).
- ⁹B. Bor, L. Heilmann, B. Domènech, M. Kampferbeck, T. Vossmeier, H. Weller, G. A. Schneider, and D. Giuntini, *Molecules* **25**, 4790 (2020).
- ¹⁰L. H. He and M. V. Swain, *J. Mech. Behav. Biomed. Mater.* **1**, 18 (2008).
- ¹¹R. K. Roeder, *Characterization of Biomaterials* (Elsevier, 2013), p. 49.
- ¹²P. Stempfflé, O. Pantalé, M. Rousseau, E. Lopez, and X. Bourrat, *Mater. Sci. Eng., C* **30**, 715 (2010).
- ¹³A. J. Clancy, D. B. Anthony, and F. de Luca, *ACS Appl. Mater. Interfaces* **12**, 15955 (2020).
- ¹⁴J. Brunner, I. A. Baburin, S. Sturm, K. Kvashnina, A. Rossberg, T. Pietsch, S. Andreev, E. Sturm née Rosseeva, and H. Cölfen, *Adv. Mater. Interfaces* **4**, 1600431 (2017).
- ¹⁵N. Goubet, P. A. Albouy, A. Thompson, and M. P. Pileni, *CrystEngComm* **18**, 6166 (2016).
- ¹⁶M. P. Pileni, *Bull. Chem. Soc. Jpn.* **92**, 312 (2019).
- ¹⁷M. A. Boles and D. V. Talapin, *J. Am. Chem. Soc.* **137**, 4494 (2015).
- ¹⁸A. Travesset, *Proc. Natl. Acad. Sci. U. S. A.* **112**, 9563 (2015).
- ¹⁹B. Domènech, M. Kampferbeck, E. Larsson, T. Krekeler, B. Bor, D. Giuntini, M. Blankenburg, M. Ritter, M. Müller, T. Vossmeier, H. Weller, and G. A. Schneider, *Sci. Rep.* **9**, 3435 (2019).
- ²⁰B. Domènech, A. T. L. Tan, H. Jelitto, E. Zegarar Berodt, M. Blankenburg, O. Focke, J. Cann, C. Cem Tasan, L. Colombi Ciacchi, M. Müller, K. P. Furlan, A. J. Hart, and G. A. Schneider, *Adv. Eng. Mater.* **29**, 2000352 (2020).
- ²¹A. T. L. Tan, J. Beroz, M. Kolle, and A. J. Hart, *Adv. Mater.* **30**, e1803620 (2018).
- ²²K. E. Mueggenburg, X.-M. Lin, R. H. Goldsmith, and H. M. Jaeger, *Nat. Mater.* **6**, 656 (2007).
- ²³X. W. Gu, *JOM* **70**, 2205 (2018).
- ²⁴M.-P. Pileni, *EuroPhys. Lett.* **119**, 37002 (2017).
- ²⁵P. Podsiadlo, G. Krylova, B. Lee, K. Critchley, D. J. Gosztola, D. V. Talapin, P. D. Ashby, and E. V. Shevchenko, *J. Am. Chem. Soc.* **132**, 8953 (2010).
- ²⁶X. Qin, D. Luo, Z. Xue, Q. Song, and T. Wang, *Adv. Mater.* **30**, 1706327 (2018).
- ²⁷F. Bai, K. Bian, X. Huang, Z. Wang, and H. Fan, *Chem. Rev.* **119**(12), 7673–7717 (2019).
- ²⁸P. Podsiadlo, B. Lee, V. B. Prakapenka, G. V. Krylova, R. D. Schaller, A. Demortière, and E. V. Shevchenko, *Nano Lett.* **11**, 579 (2011).

- ²⁹B. Lee, P. Podsiadlo, S. Rupich, D. V. Talapin, T. Rajh, and E. V. Shevchenko, *J. Am. Chem. Soc.* **131**, 16386 (2009).
- ³⁰C. Yan, H. Portalès, N. Goubet, I. Arfaoui, S. Sirotkin, A. Mermet, and M.-P. Pileni, *Nanoscale* **5**, 9523 (2013).
- ³¹M. Gauvin, Y. Wan, I. Arfaoui, and M.-P. Pileni, *J. Phys. Chem. C* **118**, 5005 (2014).
- ³²M. Gauvin, N. Yang, E. Barthel, I. Arfaoui, J. Yang, P. A. Albouy, and M. P. Pileni, *J. Phys. Chem. C* **119**, 7483 (2015).
- ³³A. Çolak, J. Wei, I. Arfaoui, and M.-P. Pileni, *Phys. Chem. Chem. Phys.* **19**, 23887 (2017).
- ³⁴X. W. Gu, X. Ye, D. M. Koshy, S. Vachhani, P. Hosemann, and A. P. Alivisatos, *Proc. Natl. Acad. Sci. U. S. A.* **114**, 2836 (2017).
- ³⁵A. Dreyer, A. Feld, A. Kornowski, E. D. Yilmaz, H. Noei, A. Meyer, T. Krekeler, C. Jiao, A. Stierle, V. Abetz, H. Weller, and G. A. Schneider, *Nat. Mater.* **15**, 522 (2016).
- ³⁶B. Bor, D. Giuntini, B. Domènech, M. V. Swain, and G. A. Schneider, *J. Eur. Ceram. Soc.* **39**, 3247 (2019).
- ³⁷D. Giuntini, S. Zhao, T. Krekeler, M. Li, M. Blankenburg, B. Bor, G. Schaan, B. Domènech, M. Müller, I. Scheider, M. Ritter, and G. A. Schneider, *Sci. Adv.* **7**, eabb6063 (2021).
- ³⁸D. Giuntini, A. Davydok, M. Blankenburg, B. Domènech, B. Bor, M. Li, I. Scheider, C. Krywka, M. Müller, and G. A. Schneider, *Nano Lett.* **21**, 2891 (2021).
- ³⁹D. Giuntini, E. Torresani, K. T. Chan, M. Blankenburg, L. Saviot, B. Bor, B. Domènech, M. Shachar, M. Müller, E. A. Olevsky, J. E. Garay, and G. A. Schneider, *Nanoscale Adv.* **1**, 3139–3150 (2019).
- ⁴⁰B. Domènech, A. Plunkett, M. Kampferbeck, M. Blankenburg, B. Bor, D. Giuntini, T. Krekeler, M. Wagstaffe, H. Noei, A. Stierle, M. Ritter, M. Müller, T. Vossmeier, H. Weller, and G. A. Schneider, *Langmuir* **35**, 13893 (2019).
- ⁴¹A. Hensel, C. J. Schröter, H. Schlicke, N. Schulz, S. Riekeberg, H. K. Trieu, A. Stierle, H. Noei, H. Weller, and T. Vossmeier, *Nanomaterials* **9**, 1230 (2019).
- ⁴²M. Li, I. Scheider, B. Bor, B. Domènech, G. A. Schneider, and D. Giuntini, *Compos. Sci. Technol.* **198**, 108283 (2020).
- ⁴³L. Han, L. Wang, J. Song, M. C. Boyce, and C. Ortiz, *Nano Lett.* **11**, 3868 (2011).
- ⁴⁴P. Georgopoulos, G. A. Schneider, A. Dreyer, U. A. Handge, V. Filiz, A. Feld, E. D. Yilmaz, T. Krekeler, M. Ritter, H. Weller, and V. Abetz, *Sci. Rep.* **7**, 7314 (2017).
- ⁴⁵J. Choi, C. M. Hui, J. Pietrasik, H. Dong, K. Matyjaszewski, and M. R. Bockstaller, *Soft Matter* **8**, 4072 (2012).
- ⁴⁶E. Tam, P. Podsiadlo, E. Shevchenko, D. F. Ogletree, M.-P. Delplancke-Ogletree, and P. D. Ashby, *Nano Lett.* **10**, 2363 (2010).
- ⁴⁷Z. Wang, A. S. S. Singaravelu, R. Dai, Q. Nian, N. Chawla, and R. Y. Wang, *Angew. Chem.* **132**, 9643 (2020).
- ⁴⁸R. Luschtinetz, J. Frenzel, T. Milek, and G. Seifert, *J. Phys. Chem. C* **113**, 5730 (2009).
- ⁴⁹C. Di Valentin and D. Costa, *J. Phys. Chem. C* **116**, 2819 (2012).
- ⁵⁰K. Sellschopp, W. Heckel, J. Gäding, C. J. Schröter, A. Hensel, T. Vossmeier, H. Weller, S. Müller, and G. B. Vonbun-Feldbauer, *J. Chem. Phys.* **152**, 64702 (2020).
- ⁵¹B. Arndt, K. Sellschopp, M. Creutzburg, E. Grånäs, K. Krausert, V. Vonk, S. Müller, H. Noei, G. B. V. Feldbauer, and A. Stierle, *Commun. Chem.* **2**, 92 (2019).
- ⁵²C. A. Schneider, W. S. Rasband, and K. W. Eliceiri, *Nat. Methods* **9**, 671 (2012).
- ⁵³A. Pineau, A. A. Benzerga, and T. Pardoen, *Acta Mater.* **107**, 424 (2016).
- ⁵⁴F. D. Gunstone, J. L. Harwood, and, and A. J. Dijkstra, *The Lipid Handbook*, 3rd ed. (CRC/Taylor & Francis, Boca Raton, FL/London, 2007).
- ⁵⁵S. Takahashi, S. Hotta, A. Watanabe, N. Idota, K. Matsukawa, and Y. Sugahara, *ACS Appl. Mater. Interfaces* **9**, 1907 (2017).
- ⁵⁶M. A. Meyers and K. K. Chawla, *Mechanical Behavior of Materials*, 2nd ed. (Cambridge University Press, 2009).
- ⁵⁷L. An, D. Zhang, L. Zhang, and G. Feng, *Nanoscale* **11**, 9563 (2019).
- ⁵⁸R. O. Ritchie, *Nat. Mater.* **10**, 817 (2011).
- ⁵⁹G. I. Barenblatt, *Advances in Applied Mechanics* (Elsevier, 1962), Vol. 7, p. 55.
- ⁶⁰M. P. Pileni, *Acc. Chem. Res.* **45**, 1965 (2012).
- ⁶¹N. Schell, A. King, F. Beckmann, T. Fischer, M. Müller, and A. Schreyer, *Mater. Sci. Forum* **772**, 57 (2013).
- ⁶²C. Bohnert, N. J. Schmitt, S. M. Weygand, O. Kraft, and R. Schwaiger, *Int. J. Plast.* **81**, 1–17 (2016).
- ⁶³J. Ast, M. Ghidelli, K. Durst, M. Göken, M. Sebastiani, and A. M. Korsunsky, *Mater. Des.* **173**, 107762 (2019).
- ⁶⁴D. Kupka and E. T. Lilleodden, *Exp. Mech.* **52**, 649 (2012).
- ⁶⁵S. Bechtel, H. Özcan, E. T. Lilleodden, N. Huber, A. Schreyer, M. V. Swain, and G. A. Schneider, *J. R. Soc., Interface* **9**, 1265 (2012).
- ⁶⁶*Dubbel: Handbook of Mechanical Engineering*, edited by H. Dubbel, W. Beitz, and K.-H. Küttner (Springer, London, 1994).
- ⁶⁷I. N. Sneddon, *Int. J. Eng. Sci.* **3**, 47 (1965).
- ⁶⁸W. M. Ostachowicz and M. Krawczuk, *J. Sound Vib.* **150**, 191 (1991).